Shape Based Computer-Aided Detection of Lung Nodules in Thoracic CT Images

Xujiong Ye[1], Xinyu Lin[1], Jamshid Dehmeshki[2], *Member IEEE*, Greg Slabaugh[1], *Senior Member IEEE*, Gareth Beddoe[1], *Member IEEE*

***Abstract*—In this paper, a new CT lung nodule Computer-Aided Detection (CAD) method is proposed for detecting both solid nodules and Ground-Grass Opacity (GGO) nodules (part-solid and non-solid). This method consists of several steps. First, the lung region is segmented from the CT data using a fuzzy thresholding method. Then, the volumetric Shape Index map, which is based on local Gaussian and mean curvatures, and the "Dot" map, which is based on the Eigenvalues of a Hessian matrix, are calculated for each voxel within the lungs to enhance objects of a specific shape with high spherical elements (such as nodule objects). The combination of the shape index (local shape information) and "dot" features (local intensity dispersion information) provides a good structure descriptor for the initial nodule candidates generation. Anti-geometric diffusion, which diffuses across the image edges, is used as a preprocessing step. The smoothness of image edges enables the accurate calculation of voxel based geometric features. Adaptive thresholding and Modified Expectation Maximization methods are employed to segment potential nodule objects. Rule-based filtering is first used to remove easily dismissible non-nodule objects. This is followed by a weighted Support Vector Machine (SVM) classification to further reduce the number of false positive objects.**

The proposed method has been trained and validated on a clinical dataset of 108 thoracic CT scans using a wide range of tube dose levels which contain 220 nodules (185 solid and 35 GGO nodules) determined by a ground truth reading process. The data was randomly split into training and testing datasets. The experimental results using the independent dataset indicates an average detection rate of 90.2%, with approximately 8.2 false positives per scan. Some challenging nodules such as non-spherical nodules and low contrast part-solid and non-solid nodules were identified, while most tissues such as blood vessels were excluded. The method's high detection rate, fast computation, and applicability to different imaging conditions and nodule types shows much promise for clinical applications

***Index Terms*— Anti-Geometric Diffusion, Computer-Aided Detection (CAD), CT, Expectation-Maximization, Lung Nodule, Shape Analysis**

I. Introduction

THERE has been growing interest in the development of Computer-Tomography (CT) as a tool for detecting lung cancer. Lung nodules can be classified into two categories: solid nodules characterized by their high contrast and Ground-Glass Opacity (GGO) nodules with faint contrast and fuzzy margins [1]. Generally speaking, nodules with GGO characteristics are either part-solid (consisting of solid components and GGO components) or non-solid (pure-GGO). GGO nodules are more likely to be malignant than solid nodules [2]. Studies on lung nodule Computer-Aided Detection (CAD) are reported frequently in the literature [3]-[17]. However, most attention has been given to solid nodule detection. As pointed by Sluimer *et al*. in a review of computer analysis of CT lung scans [11], research leading to improved detection of GGO nodules should have top priority. Recently, there are a number of papers that describe GGO nodule detection. But most of the work focuses on detection with high-dose CT imaging. As discussed in [2], lung cancer screening using low-dose CT (LDCT) has been reported to be effective at detecting lung cancer. This paper describes a new CT lung CAD method that aims to detect both solid nodules and GGO (part-solid or non-solid) nodules using a range of tube dose levels.

A. Previous Work on Nodule Detection

Existing approaches in the literature for detecting potential nodules can be roughly categorized into intensity- and model-based detection methods. Intensity based detection methods are usually based on the assumption that lung nodules have relatively higher intensity than those of lung parenchyma and employ techniques such as multiple thresholding [3]; clustering [4]; artificial neural networks [5]; and mathematical morphology [6], to identify nodules in the lung area.

For model-based detection methods, techniques such as template-matching [7][8], object-based deformation [9], and the anatomy-based generic model [10] have been proposed to separate spherical shaped nodules from elongated structures such as blood vessels. Lee *et al.*[7] proposed a Genetic Algorithm (GA) Template Matching (GATM) technique for detecting nodules within the lung area. Shape and gradient features rules were used to reduce FPs. They achieved 72% sensitivity with 31 FP/ scan. Farag *et al.*[8] proposed a similar GATM approach based on Gaussian templates, while the Gaussian parameters were automatically estimated from the given data. They achieved the detection rate of 82.3% with the FP rate of 9.2%.

Recently, several approaches to lung CAD that combine geometric and intensity models to enhance local anatomical structure (e.g spherical objects) have been proposed. Paik *et al.* [13] proposed surface normal overlap (SNO) method to capture the concentration of normals by calculating derivatives of

Manuscript received September 16, 2008.

[1]Xujiong Ye, Xinyu Lin, Greg Slabaugh and Gareth Beddoe are employed by Medicsight PLC, 66 Hammersmith Road, London, W14 8UD, UK. (xujiong.ye@medicsight.com).

[2]Jamshid Dehmeshki was with Medicsight PLC and is now a Professor at the Digital Imaging Research Centre, Kingston University, London.

intensity images. They report results on 8 chest datasets with 90% sensitivity and 5.6FP/scan for solid nodules. Zhang *et al.*[14] integrated surface curvature features into the voting procedure of normal overlap. They tested on 42 thoracic CT cases and showed improvement compared to the original SNO method, with sensitivity of 92% at the same false positive rate. Mendonca *et al.*[15] also analyzed surface curvature by using the eigenanalysis of the curvature tensor to detect nodules, which achieved a sensitivity of 67.5% at 9.3 FP/scan (for nodules above 4mm) on 50 low-dose images. Pereira *et al.* [16] extracted a set of rotation invariant features from a multi-scale and multi-orientation filter bank and those features were then used in a multi-classifier for the false positive reduction.

Most of the above algorithms have been developed for solid nodules. For detection of GGO nodules, Kim *et al.*[12] used texture features and a three-layered neural network to detect GGOs. They tested on 14 scans with tube dose from 200mA to 400mA and achieved a sensitivity of 94.3%. Zhou *et al.*[17] developed a boosting k-NN classifier for automatic detection of GGO. The detected GGO region was then automatically segmented by analyzing the texture likelihood map. They applied their method to chest CT with 10 GGOs. The method detected all of the 10 nodules with only one false positive.

Despite much effort being devoted to the computer-aided nodule detection problem, lung CAD systems remain an ongoing research topic [18]. One of the major difficulties is the detection of GGO nodules with low-dose thin-slice CT screening. Another two difficulties are the detection of nodules that are adjacent to vessels or the chest wall when they have very similar intensity; and the detection of nodules that are non-spherical in shape. In such cases, intensity thresholding or model based methods might fail to identify those nodules.

B. Our Approach

This paper proposes a new and effective approach to lung CAD by calculating 3D local geometry and statistical intensity features for potential solid and GGO nodule detection. It aims to build a unified lung CAD framework with clinically acceptable performance for the detection both of solid and GGO nodules using a wide range of tube dose levels. The main contributions of the paper are summarized below:

- A unified lung CAD framework for the detection of solid and GGO nodules using a wide range of tube dose level (e.g. 30mA—250mA). Incorporating GGO detection into a lung CAD framework has great potential for clinical application.
- The components of our algorithm utilize some existing methods in new ways. In particular, new efforts have been made to adapt the methods into our lung CAD framework as follows:
  - An adaptive fuzzy thresholding method is presented for the segmentation of the lung region.
  - The application of anti-geometric diffusion [19] to the image prior to computing geometric features. The smoothness of the edges generated by anti-geometric diffusion is better suited to the accurate calculation of the voxel based features (such as shape index features).
  - The combination of features is well suited to detect solid and GGO nodules. In particular, the shape index [20] (local shape information) and "dot" features [21] (local intensity dispersion information) provide a good structure descriptor that can detect most of the nodules.
  - The accurate segmentation of the nodule object is very important for the extraction of features. Our solution to efficiently segment the potential nodule object involves two steps: a) an adaptive thresholding for a coarse segmentation; b) a Modified Expectation Maximization algorithm (MEM) for accurate segmentation.

The proposed method has been evaluated on a clinical dataset of 108 thoracic CT scans with tube range from 30mA to 250mA. The experimental results demonstrate the high performance of the proposed method, with an overall detection rate of 90.2% (including solid and GGO nodules), false positives at approximately 8.2/scan.

II. Methodology

Fig.1 gives an overview of our proposed lung nodule detection scheme. In the following sections, each stage is described in detail.

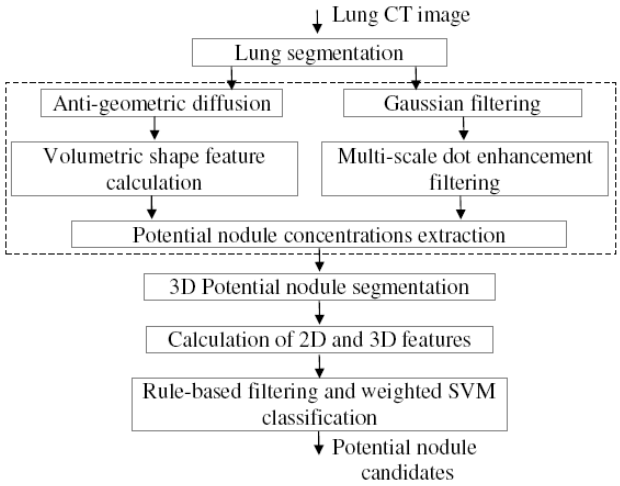

Fig.1 Block diagram of the proposed nodule detection system

A. Lung Segmentation

Due to the different scanning protocols, it is challenging to choose a threshold for lung image segmentation. Vinhais *et al.* [22] presented a fully automated method for extracting the lung region based on material decomposition. They applied the method on 30 thoracic CT images and it provided a reproducible set of thresholds for accurate extraction of the lungs. Hu *et al.*[23] used optimal thresholding to automatically segment lungs.

In this paper, a two-step segmentation method is proposed for lung extraction. First, a 3D adaptive fuzzy thresholding [24] is used to obtain the initial lung mask; then a 2D-based post-refinement process on the lung contour chain code is applied to obtain a complete lung mask; both described below.

Let $T_{low}(i)$ and $M_{low}(i)$ denote the cumulative histogram and first moment starting from the minimum intensity $I_{\min}$ of the image, respectively; while $T_{high}(i)$ and $M_{high}(i)$ starting from the maximum intensity $I_{\max}$. In this paper, to exclude the voxels outside the thorax, a simple thresholding (e.g. -1000HU) is first applied on the whole image to produce a processing mask image. $I_{\min}$ and $I_{\max}$ are then the minimum and maximum grey

level of the original image over the voxels in the mask.

Given a particular gray level *i*, the histogram can be divided into two regions. For each of the two regions, the mean value can be calculated as:

$$\mu_{low}(i)=\frac{M_{low}(i)}{T_{low}(i)}\,,\ \mu_{high}(i)=\frac{M_{high}(i)}{T_{high}(i)} \tag{1}$$

In order to determine an optimum threshold, a cost function is calculated at each grey level *i* [24],

$$C_i=\sum_{t=0}^{L-1}\left[m_i(t)*(1.0-m_i(t))\right]^2 \tag{2}$$

where $m_i(t)$ is a membership measurement at each grey level *t* to one of two regions separated in the histogram by the grey level *i*. The closer the data point (*t*) is to the mean of its region, the higher its membership value. The gray level I_0 that provides a minimum cost function is chosen as a threshold for 3D lung image segmentation.

Based on the threshold I_0, the initial thorax object is identified from the original CT image. A morphological flood fill operation [25] is then used to obtain a hole-free lung mask. Fig.2 (b) shows an example of the initial segmented lung mask from the first step of the lung extraction. It is noted that a nodule attached to the lung wall and some other attached tissues such as vessels are initially excluded from the lung mask at this step.

The aim of the second step of the lung extraction process is to obtain those attached objects. For each 2-D slice of the segmented lung object, a chain code [25], is employed to represent the initial lung contour. Alternatively, each code can be considered as an angular direction, in multiples of 45 degrees. 1-D Gaussian smoothing is then applied to the chain codes to remove the noise from the initial lung contour. By specifying a threshold value on the smoothed angle code (e.g.180), each point can be classified as a concave point (above 180), or a convex point (below 180), or a smooth point (180). A concave section is specified by its critical points (such as A and B in Fig. 3). These points are detected by examining the chain code and identifying each transition point for which the angle increases [26]. By using this chain code representation, the pairs of critical points are then detected on each segmented lung slice. The next step of the lung contour refinement is to join corresponding pairs of critical points and fill in the resulting polygons formed by all the points in the contour in between the pair of critical points, which are endpoints of a concave region. Fig.2(d) shows the final segmented lung image. The subsequent nodule detection is calculated within the segmented lung mask.

B. Potential Lung Nodule Concentrations Extraction

The volumetric shape index [20] is a measure of local shape characteristics. Given the fact that a nodule is generally either spherical or has local spherical elements, while a blood vessel is usually oblong, the volumetric shape index, which identifies spherical elements, can be used as the first step to detect potential nodule candidates. It is noted that, compared to solid nodules, GGO nodules have irregular shapes and vague boundaries. In this paper, it is assumed that there are some spherical elements embedded in those irregular shapes. We define *spherical elements* as a local grouping of voxels recognized by high volumetric shape index values. For example, while a GGO nodule may not be entirely spherical, it can still be detected by identifying small spherical elements concentrated within the GGO object. The goal in this section is to detect the potential nodules based on these spherical elements. In the next section, we will address the complete segmentation of potential nodules. An example of pure GGO using spherical elements concentrated in parts of the object is given in Fig.7.

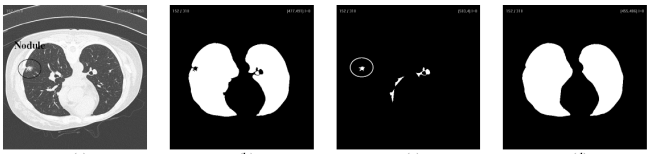

Fig.2 Lung segmentation based on a fuzzy thresholding method; processing goes from left to right. (a) Original CT lung image; (b) Lung mask extraction from fuzzy thresholding; (c) Segmented concave regions (an attached nodule and other attached tissues) based on critical points; (d) Final segmented lung mask formed by adding the (b) and (c) to produce the final lung mask.

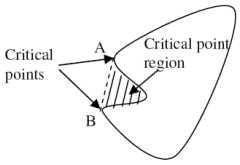

Fig.3. Lung post-processing based on critical points

In this subsection, an anti-geometric diffusion model, proposed by Manay *et al.* [19] is used prior to the shape index calculation. This model differs from Gaussian smoothing suggested in [27] or geometric diffusion models (including anisotropic diffusion) introduced by Perona and Malik [28] for image smoothing and denoising. The anti-geometric diffusion model diffuses across image edges. The advantages of diffusing across image edge include better localization, less sensitivity to noise, and better connectivity of the shape index map.

1) Pre-Processing using Anti- Geometric Diffusion

The anti-geometric diffusion model was introduced in the context of adaptive thresholding and fast segmentation [19]. A brief description of this method is as below.

Given the iso-intensity contours of an image $I(x, y, z)$, let η and ξ denote the gradient and the tangent directions, respecitively. Recall that the linear heat equation is described as $\frac{\partial I}{\partial t}=\nabla\cdot\nabla I=I_{\zeta\zeta}+I_{\eta\eta}$. In the case of anti-geometric diffusion, the tangential diffusion is excluded and only the normal diffusion is applied, the anti-geometric diffusion is defined as:

$$\frac{\partial I}{\partial t}=I_{\eta\eta}=\frac{I_x^2I_{xx}+2I_xI_yI_{xy}+I_y^2I_{yy}}{I_x^2+I_y^2} \tag{3}$$

where, I_x and I_y are the first derivatives along x and y.

The result of diffusion in the normal direction is that the image edges are smeared. The smoothness of the edge is very important for accurate voxel based geometry feature calculation (such as shape index). This will be discussed in the next subsection, where examples of shape index calculation on one GGO nodule with different diffusion models are also given for comparison.

2) Shape Index: A 3D Geometric Feature

The volumetric shape index (SI) at voxel $p(x, y, z)$ can be defined as [20][27]:

$$SI(p) = \frac{1}{2} - \frac{1}{\pi} \arctan \frac{k_1(p) + k_2(p)}{k_1(p) - k_2(p)} \quad (4)$$

where $k_1(p)$ and $k_2(p)$ are principal curvatures at voxel p.

Every distinct shape, except for the plane, corresponds to a unique shape index [20]. Five well-known shape classes have the following shape index values: cup (0.0), rut (0.25), saddle (0.5), ridge (0.75), and cap (1.0). For example, the shape index value is 1.0 indicates a sphere-like shape which represents a "cap", and 0.75 indicates a cylinder-like shape which represents a "ridge". Volumetric shape index directly characterizes the topological shape of an iso-surface in the vicinity of each voxel.

To illustrate the characteristics of the shape index, Fig.4(a) shows an example of one small lung nodule attached to a blood vessel. It is noted that different shape index values between the sphere-like nodule and the cylinder-like blood vessel at each voxel are obtained; the average of shape index values for the nodule is higher than that for the blood vessel.

Figure 5 demonstrates the influence of the different diffusion models on the shape index calculation of a GGO nodule. It can be seen that, by using the anti-geometric diffusion, the average shape index value at voxels close to nodule edge are higher than that of geometric diffusion or Gaussian smoothing. This is because the anti-geometric diffusion smears the image edge, providing better localization and connectivity of the shape index at nodule edges. Later, in the Section III of this paper, we will present results showing that the use of anti-geometric diffusion in the overall CAD system yields better performance than the use of Gaussian smoothing as a pre-processing step.

3) Potential Nodule Candidates Detection Based on the Shape Index Feature

A sphericity region is defined as a region for which, for $\forall i, j \in \Re_s$, (i, j are 3D connected voxels) we have:

$$SI(i) \geq \vartheta_1, SI(j) \geq \vartheta_1 \quad (5)$$

where ϑ_1 is a high shape index threshold chosen experimentally. In this paper, we refer to clusters of spherical elements as potential nodule concentration regions, which can be extracted using the following steps:

- Based on the calculated shape index map using (4), all the high sphericity regions ($\cup \Re_{sh}$) that satisfy the condition set in (5) are identified, with $\vartheta_1 \in [0.9,1]$. The size of each $\Re_{sh}$ is set to be larger than δ_1 voxels. Fig.6(b) is the detected high sphericity concentration regions with ϑ_1 and δ_1 chosen to be 0.92 and 3.
- Find all the low sphericity regions ($\cup \Re_{sl}$) that satisfy (5) with $\vartheta_1 \in [0.8,0.9)$. The size of each $\Re_{sl}$ is set to be larger than δ_2 voxels. Fig.6 (c) is the detected low sphericity regions with ϑ_1 and δ_1 chosen to be 0.82 and 20.
- The region $\Re_{sl}$ is regarded as a potential nodule region if the region $\Re_{sl}$ contains at least one high sphericity region $\Re_{sh}$ as $\Re_{sh} \subset \Re_{sl}$. Fig.6(d) shows an example of the detected potential nodule regions.

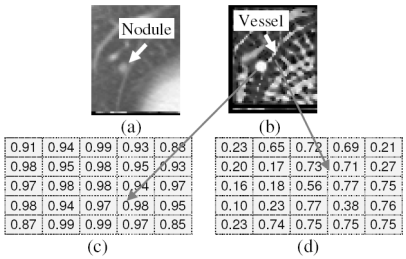

Fig.4. Shape index map with a nodule attached to a vessel. (a) Original CT image; (b) Shape index map; Shape index map values for the nodule (c) and for the blood vessel (d).

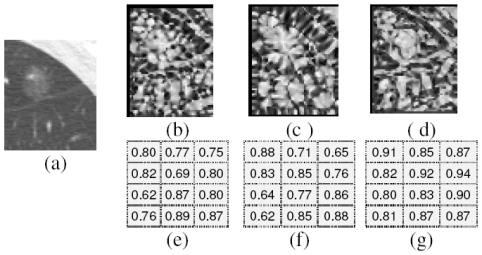

Fig.5. Shape index maps produced using different diffusion models. (a) One slice of a GGO nodule; Shape index map with Gaussian smoothing ($\sigma = 1.0$) (b) Geometric diffusion ($\Delta t = 1.0$) (c) and anti-geometric diffusion ($\Delta t = 1.0$) (d); (e)~(g) Example of corresponding shape index values at the same voxels adjacent to the nodule edge.

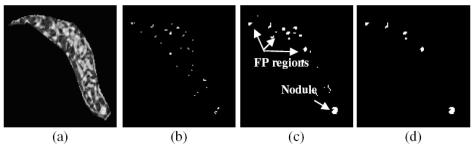

Fig.6. An example of solid nodule regions extraction. (a) shape index map; (b) high sphericity regions; (c) low sphericity regions; (d) detected potential nodule candidates from step (3).

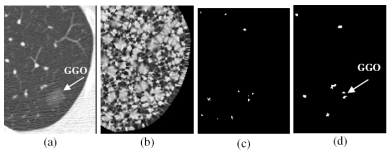

Fig.7. An example of pure GGO nodule regions extraction. (a) GGO sub-image; (b) shape index map of the GGO; (c) high sphericity regions; (d) detected potential nodule candidates from step (3).

Fig.6 and Fig.7 are the examples of potential nodule concentration extraction based on the shape index for both solid and GGO nodules. Compared to the nodule concentration in Fig.6(d) for the solid nodule which the spherical elements covers most of the nodule object, the high spherical elements shown in Fig.7(d) only cover a small part of the GGO. This demonstrates that, although the GGO nodules have irregular shapes and vague boundaries, they still contain small spherical elements that can be detected by the shape feature.

4) Multi- Scale Dot Enhancement Filtering

The Dot enhancement (DE) algorithm can be used to enhance the objects of a specific shape (such as dot-like nodule objects). For each voxel, the Dot value is defined as [21]:

$$Z_{dot}(\lambda_1, \lambda_2, \lambda_3) = \begin{cases} |\lambda_3|^2 / |\lambda_1| & \text{if } \lambda_1 < 0, \lambda_2 < 0, \lambda_3 < 0 \\ 0 & \text{Otherwise} \end{cases} \quad (6)$$

where λ_1, λ_2 and λ_3 ($|\lambda_1| \geq |\lambda_2| \geq |\lambda_3|$) are three eigenvalues of the Hessian matrix calculated from second derivatives of image.

To reduce the effect of the noise and also to take into account different object sizes, Gaussian image smoothing with a variety of scales is performed prior to the calculation of the second derivatives. Assuming that the diameters of nodule objects to be enhanced are in a range $[d_0, d_1]$ (e.g [2mm, 20mm]), the N discrete smoothing scales (σ_N) in the range of $[d_0/4, d_1/4]$ can be calculated as:

$$\sigma_1 = d_0/4,\ \ \sigma_2 = r\sigma_1,\ \ \ldots,\ \ \sigma_N = r^{N-1}\sigma_1 = d_1/4 \qquad (7)$$

where $r = (d_1/d_0)^{1/(N-1)}$. It is noted that image resolution is considered in the calculation of Gaussian smoothing with different scales and each of the enhancement filters enhances objects with a specific scale. The maximum Dot value calculated using (6) among the different scales (7) is chosen to be the final dot value for each voxel in the Dot map.

In this paper, the Dot map is calculated on each CT sub-image, which contains one potential nodule region $\Re_{sl}$. Three Gaussian scales are used to remove the noise. The region is kept as a potential nodule candidate if the number of voxels whose Dot values are larger than a pre-defined threshold. By using the Dot filtering, most of the FP regions (e.g. joint of vessel) with high spherical elements can be removed from the nodule candidates

C. 3D Potential Nodule Segmentation

In this subsection, two methods are proposed to segment the potential nodule objects: (a) Segmentation based on an adaptive thresholding; (b) Segmentation based on a Modified Expectation Maximization (MEM) algorithm. The former is an intensity-based method for fast segmentation of potential nodule objects (referred to as a coarse segmentation), especially for low contrast nodules such as GGOs; while the latter is used to segment the potential nodule objects considering the neighboring intensities (referred to as a fine segmentation).

1) Adaptive Thresholding based Segmentation

An adaptive thresholding method is applied to the extracted sub-image from the potential nodule concentration ($\Re_{sl}$) to segment the potential nodule objects. The high and low intensity thresholds can be calculated as follows:

$$f_{TL} = f_M - |f_{\min} - f_M| * 0.1,\ f_{TH} = f_{\max} + |f_{\min} - f_{\max}| * 0.1 \qquad (8)$$

where, f_M and $f_{\max}$ are the mean and maximum intensities in the region $\Re_{sl}$, respectively. $f_{\min}$ is the minimum intensity in the sub-image. Fig.8 shows a segmented potential GGO nodule based on the adaptive thresholding. A 3D region labeling technique [25] is applied on the segmented image and the 3D connected region that has the largest overlap with the concentration mask is used as the final segmented nodule object as shown in Fig.8(c).

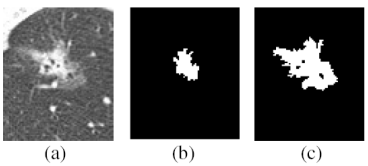

(a) (b) (c)

Fig.8. Potential nodule segmentation based on adaptive thresholding; (a) One 2D cross-section of 3D original nodule image; (b) Potential nodule concentration $\Re_{sl}$ from shape index map; (c) Segmented nodule region.

The adaptive thresholding is a fast segmentation method. Based on (8), the low threshold (f_{TL}) for the nodule segmentation is mainly estimated based on the intensity statistics (such as mean intensity) of the region concentration $\Re_{sl}$. Therefore, the algorithm can provide a better object boundary when these intensity statistics are similar to that of the segmented nodule. As discussed in the previous subsection, the region $\Re_{sl}$ represents lower sphericity concentration that is obtained from shape index map. It usually covers the core part of the segmented object. This is the main reason why this adaptive algorithm can segment most of the potential nodules that have smaller intensity variance within the nodule objects (e.g. most low contrast nodules). However, in the case of some potential nodules which have relatively larger intensity variance, the algorithm fails to properly identify the object boundary. An example can be seen in Fig.10(b), which shows underestimation of nodule boundary. To solve this problem, a MEM-based segmentation method is discussed below.

2) MEM based Segmentation

To properly segment the potential nodule object, a mixed statistical model taking into consideration spatial properties is used. This method is based on the combination of a Markov Random Field (MRF) and an Expectation–Maximization (EM) algorithm to iteratively estimate the model parameters and then calculate the probability that each voxel represents the object (potential nodule) [29]. A brief description of this method and how it is applicable to the nodule segmentation are given below.

We assume an intensity image $Y = \{y_i, i = 1,2,\ldots, M\}$ with M voxels of intensity y_i and K different classes $\hat{L} = \{1,2,\ldots K\}$. In this paper, a special case of two classes (K=2): object (potential nodule) and background, is considered. The ranges of image intensities can be modelled as Gaussian distributions with parameters $\phi_l = (\mu_l, \sigma_l)$, here $l = 1,2$:

$$p_l(y_i|\varphi_l) = G(\mu_l, \sigma_l) = \frac{1}{\sqrt{2\pi}\sigma_l}\exp\left(-\frac{(y_i - \mu_l)^2}{2\sigma_l^2}\right) \qquad (9)$$

According to the Bayesian probability theory, the posterior probability $p(\varphi_l|y_i)$ can be obtained as:

$$p(\varphi_l|y_i) = \frac{p_l(y_i|\varphi_l)\cdot p(\varphi_{l(i)})}{\sum_l p_l(y_i|\varphi_l)\cdot p(\varphi_{l(i)})} \qquad l = 1,2 \qquad (10)$$

Here, $p(\varphi_{l(i)})$ is a spatial prior probability. The spatial constraints can be imposed by a Markov Random Field (MRF) and Gibbs Random Field (MRF-GRF) [29].

The posterior probability $p(\varphi_l|y_i)$ in (10) represents the probability that the given voxel i belongs to one class $l \in \hat{L}$. In the case of nodule object segmentation, the class $l_i^* \in [1,2]$ which maximizes $p(\varphi_l|y_i)$ is chosen to be the class label for that voxel. Namely, $l_i^* = \arg\max_l p(\varphi_l|y_i)$.

Fig.9 shows an example of the potential nodule segmentation based on MEM algorithm. It can be seen that the potential nodule boundary can be properly separated from the attached blood vessel.

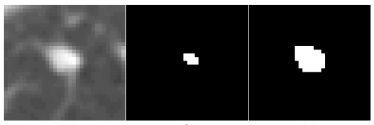

Fig.9. Potential nodule segmentation based on MEM; (a) One 2D cross-section of 3D original nodule image; (b) Potential nodule concentration $\Re_{sl}$ from shape index map; (c) Segmented nodule region.

Fig.10. A comparison of segmentation results of a non-uniform nodule based on adaptive thresholding and MEM; (a) Original nodule image; Segmented result based on adaptive thresholding (b) and based on MEM (c).

Fig.10 shows the segmentation results of a mixed GGO nodule based on the adaptive thresholding and MEM methods. In this example, it can be seen that due to the heterogeneity of the nodule, there is a "dark" area surrounding the core part (high contrast) of the nodule in Fig.10(a). Using the adaptive thresholding, those pixels in the "dark" area are wrongly identified as background so that the segmented nodule object is underestimated (Fig.10(b)); while by using the MEM algorithm, those pixels can be correctly identified as being part of the nodule object, as seen in Fig.10(c). This is because the MRF-GRF is used as a spatial constraint. The segmentation not only depends on the intensity but also the spatial information.

To speed up the overall computation time, we make use of the assumption discussed in the previous subsection that most low contrast nodules have smaller intensity variance within the nodule objects so that the fast adaptive algorithm can properly segment those potential nodules. In this paper, for each potential nodule region, the adaptive thresholding is firstly applied to obtain the initial segmented object. The intensity mean of each segmented object is then calculated. For the region that have a high intensity mean (e.g larger than -500HU), the MEM is then employed to properly segment the potential nodule object.

It is worthwhile to emphasize that, in the case of nodules with vasculature attachment, theoretically, the MEM based method which takes into account spatial information provides better segmentation results (e.g. this may separate the nodule from adjoining vessel), compared to the adaptive based method. However, for the nodule attached to the lung wall (pleural nodule), both the adaptive and MEM based methods can not properly segment those nodules. In this paper, those nodules are segmented in the process of lung segmentation; where the chain code based critical point method is used which is discussed in Section 2. An example of segmented attached nodule is shown in Fig.2(c). Below is the summary of the potential nodule segmentation.

For each potential nodule region from Section 2B:

Step 1 (Pleural nodules): If the region overlaps with a critical point region detected during lung segmentation, the potential nodule is considered to be attached to the lung wall. The critical point region is used as the segmented region.

Step 2 (Non-pleural nodules): If the nodule is not attached to the lung wall (not overlaps with a critical point region), segment the region based on the adaptive thresholding and calculate the intensity mean of the segmented region. If the mean intensity is less than -500 HU, stop; otherwise: refine the segmentation using the MEM method.

D. Local 3D Geometric Features and Rule-based Classifier

In this step, geometric features are calculated on each segmented potential nodule object. A rule-based classifier is then applied on each potential nodule object in order to quickly remove easily dismissible non-nodule objects.

1) 3D Maximum Distance based on Distance Transform

For each potential nodule object ($\Re_{seg}$), a 3D distance map is calculated based on the Euclidean distance transform [25]. Fig.11 shows an example of the distance transform map; Fig.11(c) is the corresponding distance map within the segmented object. The pixel with the highest grey leveling in Fig.11 (c) has the maximum distance to the boundary within the object. This maximum distance value can be used as one feature which represents the object thickness. This feature can be used to remove regions with small maximum distance value, which are often vessels. It is noted that, in this paper, the distance transform is calculated with consideration of the anisotropy of the image data.

Fig.11. An example of distance transform map; (a) Original sub-image; (b) Segmented object; (c) Grey-level distance transform map.

2) 3D Object Filtering Based on Motion Tracking

Assuming that the 3D potential nodule object contains more than one 2D blob (a blob is a cross-sectional object defined in x-y plane, also referred as scan plane) along the scanning (z) direction, an object is defined as a *blob-moving* object if its 2D blobs on different continuous slices are moving along the x-y plane. Blob-moving objects are typically indicative of vessels. Fig.12 shows an example of a blob-moving object.

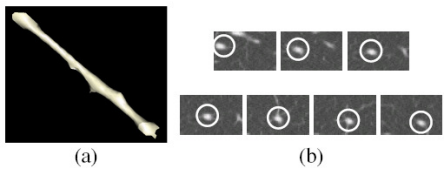

Fig.12. An example of a blob-moving object; (a) 3D view of the object (blood vessel); (b) 2D view of each blob on continuous slices (along scan direction).

The aim of the rule described in this subsection is to detect 3D blob-moving objects by calculating the overlap kernel (core) regions between the 2D blobs on consecutive slices. The 2D kernel region is calculated based on 2D distance transform. Let $\Re^i_{2DKernel}$ the kernel region of the *i*th 2D blob, for each pixel *p* in *i*th 2D blob $\Re^i_{2DBlob}$, $\forall p \in R_{seg}$ *and* $p \in R^i_{2DBlob}$, we have:

$$p \in R^i_{2DKernel} \text{ if } f_{2DDist\_p} \geq f_{2DDistMax} * k \quad (11)$$

Here, f_{2DDist_p} is the distance value at the *p*th pixel in the 2D distance map; while $f_{2DDistMax}$ is the maximum distance

value within the 2D blob in the 2D distance map, and k is a positive constant which controls the size of the core region, $k \in (0,1)$. In this paper, k is 0.6 which is determined experimentally. A brief description of how to choose an optimal value for parameter k is given in the section 2D (5).

For each 3D object $\Re_{seg}$, the kernel region of each 2D blob is calculated based on (11), then the object $\Re_{seg}$ is kept as a nodule candidate if:

$$\sum_{i=1}^{n-1} \delta\left(\left| \cap \left(R_{2DKernel}^{i}, R_{2DKernel}^{i+1} \right) \right| \right) > 0.5 * n \qquad (12)$$

where n is the total number of the 2D blobs; the operator $\cap(\cdot)$ is the AND operation: $\delta(x) = \begin{cases} 1 & \text{if } x > 0 \\ 0 & \text{if } x = 0 \end{cases}$.

That is to say, if the number of the overlap regions is less than a preset threshold (e.g. half of total number of 2D blobs), the region is defined as a 3D blob-moving object and removed from the nodule candidates.

3) Sphericity

The sphericity is defined as the ratio between the object volume size and the circumscribed (minimum enclosing) sphere volume size. The sphericity can be used to remove the 3D objects that are elongated.

4) Effective Diameter

The effective diameter is defined as the diameter of a sphere with the same volume of the segmented object. This feature is used to remove very small (e.g. 2mm or less) nodule candidates.

5) Parameter Selection

The above features are used in a rule-based classifier to remove easily dismissible non-nodule objects. Each feature is associated with one rule. The output from one rule will be employed as the input to a subsequent rule. To determine the threshold for each rule, clinical knowledge, i.e. the size of the region (e.g. 2mm), the degree of sphericity, etc, can be considered to obtain the initial threshold value; then the threshold that provides a good cutoff in ROC curve is chosen to minimize the overtraining effect for the rule-based classifier. As an example, we illustrate how to determine k in Equation 11 (Section 2D(2)). For all the potential nodule objects obtained from Section 2B, 3D filtering based on the detection of the 3D blob-moving object (Section 2D(2)) is used as one rule to remove false positive regions. Fig.13 shows the ROC curve based on different k values on 54 training scans. It can be seen that k=0.6 gives good detection performance with regards to sensitivity and false positives.

E. SVM-based Classification

The rule-based classifier is employed in order to quickly remove obvious false positive (outliers) so that their influence on the training of the second classifier was eliminated. In this subsection, a weighted support vector machine (SVM) [30] classification method is applied to further separate nodules from non-nodule candidates.

For the feature space in d-dimensions, we are given training dataset $S = (x_1, y_1), ..., (x_l, y_l)$, where $x_l \in d$, and the class label $y_l \in \{+1, -1\}$ (where +1 corresponds to a nodule and -1 to a non-nodule). The decision function of the weighted-SVM is given as [30]: $f(x) = \text{sgn}\left(\sum_{i=1}^{l} y_i a_i^* K(x, x_i) + b^* \right)$

where $K(x, y)$ is a non-linear kernel function, $b \in R$ and a is constrained as follows: $0 \le a_i \le C_+$, for $y_i = +1$, and $0 \le a_i \le C_-$, for $y_i = -1$. Where C_+ and C_- are penalties for class +1 and -1, respectively.

In this paper, the LibSVM [31] was used with a radial basis function kernel, defined as $K(x, x) = \exp\left(-\gamma \left\| x - x' \right\|^2 \right)$, for $\gamma > 0$. The input parameters are determined through 5-fold cross validation via parallel grid-search. Each subset is created based on subtractive clustering [32].

Fifteen features which are listed in Table 1 are empirically used in this study to characterize the remaining nodule candidates. All the input features are normalized to [-1, 1].

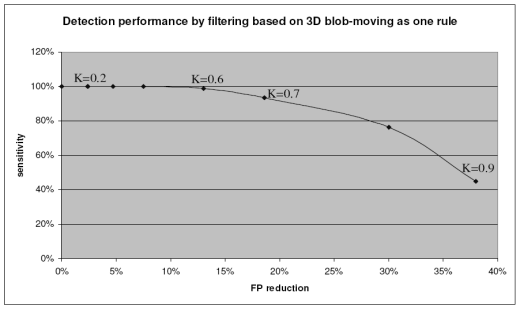

Fig.13 ROC curve on 54 training scans by using 3D blob-moving as only one rule with different k values (11). (Here, it is assumed the sensitivity before the rule filtering is 100%)

Table 1. Features for the classification

#	Feature	Definition
1-4	Max_I, Min_I, Mean_I, Std_I	Maximum, minimum, mean, standard deviation of intensity
5	Compactness	Ratio of volume equivalent radius and spatial deviation equivalent radius
6	Shape index mean	Mean of shape index map in the segmented object
7-9	Skewness, kurtosis, correlation	Those texture features calculated in grey level image by using the segmented object mask
10	Elongation	Ratio between the first and second eigenvalues
11	Volume size	Number of voxels within the segmented object multiplied by the image resolution
12	Object location	Defined as the distance to the lung contour
13-14	Sphericity and effective diameter	Defined in subsection D
15	3D maximum distance to the boundary	Defined in subsection D

III. EXPERIMENTAL RESULTS

A database of 108 thoracic CT scans from several different hospitals was used to evaluate the effectiveness of the proposed method. Slice thickness varied from 0.5mm to 2.0mm and the total slice number for each scan varied from 79 to 396 with an average of 199 per-scan. The X-ray tube current ranged from 30mA to 250mA. Among those 108 scans, 58 scans have 30mA tube current, 10 scans at 50 mA, and the rest are above 100mA. Each scan was read individually by members of a qualified panel and then a consensual gold standard was defined by the panel. This process defined ground truth of 220 nodules (185 solid nodules and 35 GGO nodules). All the GGO nodules are in the scans with 30 mA tube current.

The whole data set was processed using the method described in Section II. Potential nodule candidates were first generated based on shape index features, where the high shape index threshold ϑ_1 in Equation 5 was set to be 0.91 with size threshold δ_1=3. A ROC curve with different ϑ_1 is also given in Fig.17 in the discussion section, which indicates ϑ_1=0.91 provides an optimal overall performance regarding to the sensitivity and false positives. The low shape index threshold in Equation 5 was 0.82 with δ_2=12; the "dot" filtering was then used to remove FP regions, 3-scales Gaussian with σ_1=0.5mm, σ_2=1.6mm; σ_3=5mm (in Equation 7), were used to remove noise. For each region from shape index, if the total number of 3D connected voxels with high dot value are larger than 6, the region is kept as a potential nodule region. By using this dot filtering, in total, 4639 nodule candidates were generated at the initial stage (4419 non-nodule regions and 220 nodule regions). The dataset was randomly split into training and testing datasets with the same number of scans (54 scans each). The latter was used as the independent testing for evaluating the performance of the trained classifiers, which has 2393 nodule candidates. This includes 122 nodule regions (104 solid nodules and 18 GGO nodules) and 2271 non-nodule regions.

For the training dataset, the rule based classifier was firstly used to remove easily dismissible false regions. As discussed in the parameter selection Section 2D (5), the parameter for each rule that provides good cutoff in an ROC curve is chosen to minimize the overtraining effect for the rule-based classifier. For example, the threshold for the sphericity filtering in Section 2D (3) is set to be 0.8. The threshold for the effective diameter is chosen to be 2mm. After the rules filtering, for the remaining nodule candidates, the weighted SVM was then employed to further remove false positive regions.

The weighted SVM was trained using the following scheme. Subtractive clustering was used to estimate the number and location of cluster centres in the training dataset. 5-fold cross-validation (with roughly equal sized folds) was performed based on the results of the subtractive clustering. Due to the imbalanced data, and to reduce the computational cost, for each fold, the non-nodule regions (majority class) were randomly down-sampled to 5 times of the number of the nodule regions (minority class). The model was trained 5 times, each time leaving out one of the folds from the training.

Table 2 shows final nodule detection performance (after rule-based filtering and the weighted-SVM) on the training scans. It can be seen that 93 (78 solid and 15 GGO nodules) out of the total 98 nodules (81 solid and 17 GGO nodules) were detected by the proposed method, resulting the average detection rate of about 95%, with the FP rate of 6.2/scan.

The trained model was tested on the independent data. Table 3 shows the results of the rule based classifier applied to 54 independent testing scans. The first row of the Table is the detection performance for the solid nodules; while the second row of the table is for the GGO nodules. The remaining nodule candidates (1068 regions in total) are then fed into the weighted-SVM for the further reduction. Table 4 shows the performance of the trained weighted SVM on independent data. As it can be seen that, 95 out of 101 solid nodules are detected by the weighted-SVM resulting the sensitivity of 94%, while 15 of 17 GGO nodules can be found with the sensitivity of 88.2%. 1828 non-nodule regions were removed from the candidates, resulting the final average FP at about 8.2/scan.

Table 5 shows the final detection sensitivity based on the different nodule size groups for the solid and GGO nodules, by using the proposed method on the independent testing data.

Table 2. Detection performance of the trained models (rule based filtering and the weighted-SVM) on the training dataset (54 scans with 98 nodules)

Total nodule	*Nodule detected*	*Detection rate*	*FP Per-scan*
98	93	95%	6.2/scan

Table 3. Detection performance for the rule based classifier on the independent dataset (54 scans with 122 nodules)

Nodule type	*Total nodule*	*Nodule detected*	*Detection rate*	*FP Per-scan*
Solid nodule	104	101	97.1%	17.6/scan
GGO nodule	18	17	94.4%	17.6/scan

Table 4. Detection performance for the weighted-SVM on the independent dataset (54 scans with 118 nodules, including 101 solid and 17 GGO).

Nodule type	*Total nodule*	*Nodule detected*	*Detection rate*	*FP Per-scan*
Solid nodule	101	95	94%	8.2/scan
GGO nodule	17	15	88.2%	8.2/scan

Table 5. Sensitivity of the proposed method based on the different nodule sizes on independent testing data

Nodule Type	*<=5mm*	*5-10mm*	*10-20mm*	*Total*
Solid nodule	86.8% (33/38)	94.5% (52/55)	91% (10/11)	91.3% (95/104)
GGO nodule	- -	84.6% (11/13)	80% (4/5)	83.3% (15/18)

Table 6. Comparison of detection performances with Gaussian smoothing and anti-geometric diffusion followed by the rule based filtering and the weighted SVM on the independent dataset (54 scans) containing 122 nodules

	Nodule detected	*Detection rate*	*FP Per-scan*
Gaussian based method	96	78.7%	12.7/scan
Anti-geometric based method	110	90.2%	8.2/scan

In the second experiment, the detection performances of different pre-processing methods were evaluated (Table 6). Two smoothing methods were used: Gaussian smoothing and the proposed anti-geometric diffusion. The first row of the Table shows the final nodule detection results with using Gaussian smoothing as a pre-processing step on independent testing data (54 scans), where 96 out of the 122 (78.7%) nodules were detected, with an average FP rate of 12.7/scan. For comparison, the second row of Table 6 gives the results of the whole proposed method on the same independent testing data. As indicated in Table 4, 110 (among which, 95 solid and 15 GGO nodules) of the 122 nodules were detected, with the average detection rate of 90.2%. These results demonstrate that by using the anti-geometric diffusion pre-processing, the sensitivity of the nodule detection rate increases from 78.7% to 90.2%, while the FP reduces from 12.7/scan down to 8.2/scan. Some vascular nodules or pleural nodules (such as those shown in Fig.14), were missed when Gaussian pre-processing was used, but can be detected with the proposed algorithm.

Fig.15 shows examples of different types of detected nodules. Some challenging nodules such as non-spherical nodules with spherical elements, as shown in Fig.15 (a)~(c), or attached nodules with similar intensity shown in Fig.15 (d)~(f) can be detected with the proposed shape based method.

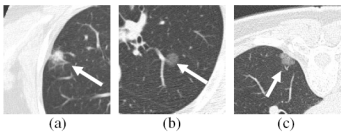

Fig.14. Nodules detected by using anti-geometric diffusion pre-processing (and missed with Gaussian smoothing).

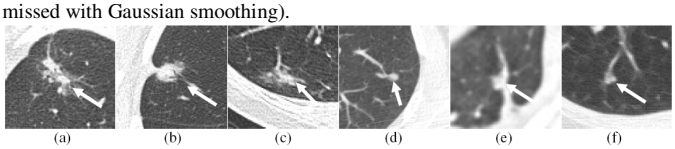

Fig.15. Different types of nodules detected with the proposed method. (a)~(c) non-spherical nodules; (d)~(f) nodules attached to vessels with similar intensity.

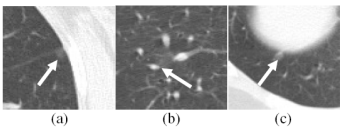

Fig.16. Example of nodules missed by the proposed method

As discussed in Section II, a high spherical concentration can be obtained by thresholding the shape index map as in (5). Therefore, different shape index thresholds produce different nodule detection performances. Fig.17 shows the detection performance curves with regards to the different shape index thresholds, in which 11 sets of high shape index thresholding values were used, ranging from 0.89 to 0.99. It is noted that, a shape index thresholding value ϑ_1 of 0.91 provides an optimal overall performance with a higher detection rate (about 90.2%) and a relatively smaller FP rate (about 8.2/scan).

The proposed CAD algorithm was tested on the computer with 2.39GHz CPU and 2GB Memory. On average, it takes about 2.5mins/scan. Table 7 shows the average computation time required for each major step. Since our objective is to build a commercial lung CAD system, the fast computation time is important for the practicality of the method for clinical application.

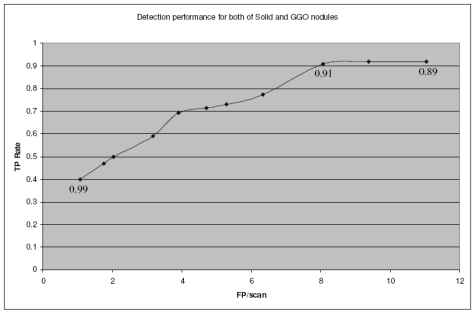

Fig.17. Performance evaluation with different high shape index thresholding values ranging from 0.89 to 0.99

Table 7. The average computation time (in seconds) at each major step

Lung segmentation	*Candidate generation based on SI*	*3-scales Dot filtering*	*Potential nodule segmentation*	*Feature calculation and filtering*
38s	28s	32s	25s	28s

IV. DISCUSSION

The result in Fig.17 shows a optimal detection rate of 90.2% (110 out of total 122 nodules detected including solid and GGO nodules) for the whole proposed method using the independent dataset. Examples of different types of detected nodules are shown in Fig.14 and Fig.15. As mentioned before, one advantage of the local shape feature is that it characterizes the local geometric feature and favors regions with high spherical elements. This is the main reason that the proposed algorithm is able to detect not only spherical nodules, but also non-spherical nodules with aspects of high local spherical elements. The second advantage of using the shape index is that, theoretically, it only represents the local shape feature, while being independent of the image intensity. This is one of the reasons why low contrast GGO nodules can be detected using the proposed system.

Some examples of nodules missed (false negatives) by the proposed method are shown in Fig.16. Typically, these nodules are very low contrast or close to the chest wall. The shape index favors regions with high spherical elements. However, nodules could be missed if they do not include local spherical elements or if the sizes of the elements are too small.

As mentioned in the beginning of Section 3, there are 68 scans with low tube current, among which 58 scans are at 30mA, and 10 scans are at 50 mA. By using the proposed method, for the scans at 30mA, the average detection sensitivity is 91.7% with FP rate of 8.6/scan; while for the scans at 50 mA, the average detection sensitivity is 90.6% with FP rate of 6.5/scan. For low dose screening, most CAD schemes in the literature are developed for thick-slice CT images, e.g. slice thickness 10mm. There are only a small number of papers that describe the detection with low-dose and thin-slice data. Mendonca *et al.* [15] applied the curvature tensor method on 50 low-dose CT scans at 40mA with reported sensitivity of 67.5% (for the nodules above 4mm) and false rate at 9.3FP/scan. By using the same low-dose data, they compared their method with the Hessian method proposed by Sato *et al.* [33], at the same rate of 9.3FP/scan, the Hessian method achieved a sensitivity of 40%. They also applied their method on 192 low-dose scans at 20mA with sensitivity of 62.9% at 10.3FP/scan. Although the databases are different, the performance of our proposed method on the low dose data indicates the effectiveness of the method with low-dose CT screening. We attribute the ability of our method to handle low dose data to the anti-geometric diffusion, which is used as a pre-processing step to remove noise and provides a good base for the accurate calculation of shape index features. In addition, the "dot" feature is calculated on multiple scales of Gaussian smoothed images. However, very noisy reconstructed images due to very low-dose tube current might lead to inaccurate calculation of the local shape feature. To further improve the detection performance, an adaptive smoothing method needs to be further investigated.

By using the proposed method, Table 8 shows the variation in sensitivity and false positive rate over all cases on the independent testing data. As it is known that different imaging parameters (e.g. different slice thickness and different tube currents) may affect the nodule detection performance, the proposed method tries to limit the influence by tuning the model (choosing the optimal parameters) on a wide range of nodules with different sizes, slice thickness and radiation. The experimental results on the independent dataset demonstrate the generalizability of the proposed method.

Table 8 The variation of nodule detection performance over all cases on independence testing data based on the proposed method. ([] indicates the number of the detected nodules among the total nodules in one scan.)

	Highest	*Lowest*	*STD*
Sensitivity	[8/8]100%	[1/2]50%	10.3
False Positive	15	1	4.96

V. CONCLUSION

This paper proposed a new approach to lung CAD by calculating 3D local geometric and statistical intensity features for potential solid and GGO nodule detection. The method has been built in a commercial lung CAD system. The experimental results demonstrate the high nodule detection performance of the proposed algorithm, with an overall detection rate of about 90.2% (including solid and GGO nodules), and FP at 8.2/scan. Despite some challenging nodules such as non-spherical, low contrast part-solid, and non-solid nodules, the detection sensitivity is high with a low rate of FP regions. Most of the tissues (blood vessels, apical scarring, etc) can be excluded as nodule candidates. The method's high performance for the detection both of solid and GGO nodules, applicability to different tube currents, and fast computation time shows much promise for clinical applications.

REFERENCES

[1] H.A.Bastawrous, T.Fukumoto, N.Nitta and M.Tsudagawa, "Detection of Ground Glass Opacities in Lung CT Images using Gabor Filters and Neural Networks", Proc. Intl., on Instrumentation and Measurement Technology (IMTC), pp.251-256, 2005.

[2] S. Chong, K.S.Lee and M.L.Chung, T.S.Kim *et al.*, "Lung cancer screening with low-dose helical CT in Korea: Experiences at the Samsung medical center", J.Korean Med Sci; 20: 402-8, 2005.

[3] S.G. Armato, M. L. Giger and H. MacMahon, ''Automated detection of lung nodules in CT scans: Preliminary results'', Medical Physics, vol.28, pp.1552–1561, 2001.

[4] M. Gurcan, B. Sahiner and N. Petrick, *et al.* "Lung nodule detection on thoracic computed tomography images: preliminary evaluation of a computer-aided diagnosis system", Medical Physics, vol.29, pp.2552-2558, 2002.

[5] K. Suzuki, S. G. Armota, F. Li, S. Sone and K. Doi, "Massive training artificial neural network (MTANN) for reduction of false positives in computerized detection of lung nodules in low-dose computed tomography", Medical Physics, vol.30, no.7, pp.1602-1617, 2003.

[6] K. Awai, K. Murao, A. Ozawa, M. Komi, H. Hayakawa, S. Hori, and Y. Nishimura, "Pulmonary nodules at chest CT: effect of computer-aided diagnosis on radiologists' detection performance", Radiology, vol.230, no.2, pp.347-352, 2004.

[7] Y. Lee, T. Hara and H. Fujita, S.Itoh, and T.Ishigaki, "Automated detection of pulmonary nodules in helical CT images based on an improved template-matching technique", IEEE Trans. on Medical Imaging, vol.20, no.7, pp.595-604, 2001.

[8] A. Farag, A. El-Baz, G.G.Gimelfarb, R. Falk and S.G. Hushek, "Automatic detection and recognition of lung abnormalities in helical CT images using deformable templates", Lecture Notes in Computer Science, Springer-Verlag, Medical Image Computing and Computer-Assisted Intervention, vol.3217, pp.856-864, 2004.

[9] Z.Y. Ge, B. Sahiner, H. P. Chan, L. M. Hadjiiski, P. N. Cascade, N. Bogot, E. A. Kazerooni, J. Wei and C. Zhou, "Computer-aided detection of lung nodules: False positive reduction using a 3D gradient field method and 3D ellipsoid fitting", Medical Physics, vol. 32, 2443, 2005.

[10] M. S. Brown, M. F. McNitt-Cray, J. G. Golldin, R. D. Suh, J. W. Sayre, and D. R. Aberle, "Patient-specific models for lung nodule detection and surveillance in CT Images", IEEE Trans. Medical Imaging, vol.20 no.12, pp1242-1250, 2001.

[11] I.Sluimer, A.Schilham, M.Prokop and B.V.Ginneken, "Computer analysis of computed tomography scans of the lung: A survey", IEEE Trans. Medical Imaging, vol.25, no.4, pp.385-405, 2006.

[12] K.G.Kim, J.M.Goo, J.H.Kim, H.J.Lee, B.G.Min, K.T.Bae, "Computer-aided diagnosis of localized ground-glass opacity in the lung at CT: Initial Experience", Radiology, 237:657-661, 2005.

[13] D.S.Paik, C.F.Beaulieu, G.D.Rubin, B.Acar, R.B.Jeffrey, J.J.Yee, J.Dey and S.Napel, "Surface normal overlap: a computer-aided detection algorithm with application to colonic polyps and lung nodules in helical CT", IEEE Trans. Medical Imaging, vol.23, no.6, 2004.

[14] X.Zhang, J.Stockel, M.Wolf, P.Cathier, G.Mclennan, E.A.Hoffman and M.Sonka, "A new Method for spherical object detection and its application to computer aided detection of pulmonary nodules in CT images", MICCAI 2007, pp.842-849.

[15] P.R.S.Mendonca, r.Bhotika, S.A.Sirohey, W.d.Turner, J.V.Miller and R.S.Avila, "Model-based analysis of local shape for lesion detection in CT scans.", MICCAI 2005, pp.688-695.

[16] Carlos Pereira, Luis Alexandre, Ana Maria Mendonça, Aurélio Campilho, "A multiclassifier approach for lung nodule classification", LNCS 4142, pp. 612-623, 2006.

[17] J.Zhou, S. Chang, D.N.Metaxas, B.Zhao, L.H.Schwartz, and M.S.Ginsberg, "Automatic Detection and Segmentation of Ground Glass Opacity Nodules", MICCAI, 2006.

[18] J. M. Goo, "Computer-aided detection of lung nodule on chest CT: issues to be solved before clinical use", Journal of Radiology, vol.6, no.2, pp.62-63, 2005.

[19] S. Manay, A.Yezzi, "Anti-geometric diffusion for adaptive thresholding and fast segmentation", IEEE Trans. Image Processing, vol.12, no.11, pp.1310-1322, 2003.

[20] O. Monga, S. Benayoun. "Using partial derivatives of 3D images to extract typical surface features", Computer Vision and Image Understanding, vol.61, pp.171-189, 1995.

[21] Q. Li, S. Sone and K. Doi, "Selective enhancement filters for nodules, vessels, and airway walls in two- and three-dimensional CT scans", Medical Physics, vol.30, no.8, pp.2040-2051, 2003.

[22] Carlos Vinhais, Aurélio Campilho, "Lung Parenchyma Segmentation from CT Images based on Material Decomposition", LNCS 4142, pp. 624-635, 2006.

[23] S.Hu, E.A.Hoffman, J.M.Reinhardt, "Automatic lung segmentation for accurate quantization of volumetric x-ray CT images", IEEE Trans. Medical Imaging, vol.20, no.6, pp.490-498, 2001.

[24] H.R.Tizhoosh, "Fuzzy Image Processing", Springer-Verlag, 1997.

[25] R.C, Gonzalez and R.E. Woods, Digital Image Processing, Addison Wesley, 2nd edition, 2002

[26] V.Alexandrov, "Using critical points in contours for segmentation of touching characters", International Conference on Computer Systems and Technologies, Rousse, Bulgaria, 2004.

[27] H.Yoshida and J. Nappi, "Three-dimensional computer-aided diagnosis scheme for detection of colonic polyps", IEEE Trans. Medical Imaging, vol.20, no.12, pp.1261-1273, 2001.

[28] P. Perona and J. Malik, "Scale –space and edge detection using anisotropic diffusion", IEEE Transactions on Pattern Analysis and Machine Intelligence, vol. 12, pp.629-639, 1990.

[29] S. Z. Li, "Markov Random Field Modeling in Computer Vision", Springer-Verlag, 1995.

[30] E.Osung and F.Girosi, "Support vector machines: Training and applications" Tech.Rep. AIM-1602, 1997.

[31] C-C.Chang and C-J. Lin, "LIBSVM: A Library for Support Vector Machine," 2006, Software available at http://www.csie.ntu.edu.tw/~cjlin/libsvm.

[32] S.Chiu, "Fuzzy model identification based on cluster estimation", *J. of Intelligent and Fuzzy Systems* 2, 267-278, 1994.

[33] Y.Sato, CF.Westin, A.Bhalerao, S.Nakajima, N.Shiraga, S.Tamura and R.Kikinis, "Tissue classification based on 3D local intensity structures for volume rendering", *IEEE Tran. Visualization and computer graphics*, vol.6, no.2, pp160-180, 2000.